



HAL
open science

Observational signatures of circumbinary discs - II. Kinematic signatures in velocity residuals

Josh Calcino, Brodie J. Norfolk, Daniel J. Price, Thomas Hilder, Jessica Speedie, Christophe Pinte, Himanshi Garg, Richard Teague, Cassandra Hall,
Jochen Stadler

► To cite this version:

Josh Calcino, Brodie J. Norfolk, Daniel J. Price, Thomas Hilder, Jessica Speedie, et al.. Observational signatures of circumbinary discs - II. Kinematic signatures in velocity residuals. *Monthly Notices of the Royal Astronomical Society*, 2024, 534, pp.2904-2917. 10.1093/mnras/stae2233 . insu-04836780

HAL Id: insu-04836780

<https://insu.hal.science/insu-04836780v1>

Submitted on 15 Dec 2024


HAL is a multi-disciplinary open access archive for the deposit and dissemination of scientific research documents, whether they are published or not. The documents may come from teaching and research institutions in France or abroad, or from public or private research centers.

L'archive ouverte pluridisciplinaire **HAL**, est destinée au dépôt et à la diffusion de documents scientifiques de niveau recherche, publiés ou non, émanant des établissements d'enseignement et de recherche français ou étrangers, des laboratoires publics ou privés.



Distributed under a Creative Commons Attribution 4.0 International License

Observational signatures of circumbinary discs - II. Kinematic signatures in velocity residuals

Josh Calcino ¹★, Brodie J. Norfolk,² Daniel J. Price ², Thomas Hilder,² Jessica Speedie,³ Christophe Pinte ^{2,4}, Himanshi Garg,² Richard Teague,⁵ Cassandra Hall ^{6,7} and Jochen Stadler ^{4,8}

¹Department of Astronomy, Tsinghua University, 30 Shuangqing Rd, 100084 Beijing, China

²School of Physics and Astronomy, Monash University, Vic 3800, Australia

³Department of Physics & Astronomy, University of Victoria, Victoria BC, V8P 5C2, Canada

⁴Univ. Grenoble Alpes, CNRS, IPAG, F-38000 Grenoble, France

⁵Department of Earth, Atmospheric, and Planetary Sciences, Massachusetts Institute of Technology, Cambridge MA 02139, USA

⁶Department of Physics and Astronomy, The University of Georgia, Athens, GA 30602, USA

⁷Center for Simulation Physics, The University of Georgia, Athens, GA 30602, USA

⁸Laboratoire Lagrange, Université Côte d'Azur, CNRS, Observatoire de la Côte d'Azur, 06304 Nice, France

Accepted 2024 September 11. Received 2024 July 30; in original form 2024 February 26

ABSTRACT

Kinematic studies of protoplanetary discs are a valuable method for uncovering hidden companions. In the first paper of this series, we presented five morphological and kinematic criteria that aid in asserting the binary nature of a protoplanetary disc. In this work, we study the kinematic signatures of circumbinary discs in the residuals of their velocity maps. We show that Doppler-flips, spiral arms, eccentric gas motion, fast flows inside of the cavity, and vortex-like kinematic signatures are commonly observed. Unlike in the planetary mass companion case, Doppler-flips in circumbinary discs are not necessarily centred on a companion, and can extend towards the cavity edge. We then compare the kinematic signatures in our simulations with observations and see similarities to the Doppler-flip signal in HD 100546 and the vortex-like kinematic signatures in HD 142527. Our analysis also reveals kinematic evidence for binarity in several protoplanetary discs typically regarded as circumstellar rather than circumbinary, including AB Aurigae and HD 100546.

Key words: hydrodynamics – methods: numerical – protoplanetary discs – circumstellar matter.

1 INTRODUCTION

A detailed analysis of the gas kinematics in protoplanetary discs has proven to be an invaluable tool for understanding the origin of the substructures often found in them (Pinte et al. 2018, 2019, 2023b; Casassus & Pérez 2019; Disk Dynamics Collaboration et al. 2020; Teague et al. 2021). Since the velocity field of the gas is a direct product of the forces acting on it, the gas kinematics are a powerful probe of the phenomena responsible for the observed substructures (e.g. Dong, Najita & Brittain 2018b; Francis & van der Marel 2020; Bae et al. 2023; Pinte et al. 2023a). Different physical phenomena can produce similar substructures in the gas and dust distribution. For example, rings and gaps seen in the mm dust continuum can be produced by planets (e.g. Dipierro et al. 2015), volatile snow lines (e.g. Zhang, Blake & Bergin 2015), the irradiation instability (Wu & Lithwick 2021; Kutra, Wu & Lithwick 2023; however, see Melon Fuksman & Klahr 2022; Pavlyuchenkov, Maksimova & Akimkin 2022), MHD driven zonal flows and winds (e.g. Suriano et al. 2018), plus many more (for a review, see Bae et al. 2023). The gas kinematics break this degeneracy as different models often predict different kinematic signatures (Pinte et al. 2023b).

Recent works have focused on understanding how forming planets produce velocity perturbations in the gas (Perez et al. 2015b; Pérez, Casassus & Benítez-Llambay 2018; Teague et al. 2018; Bollati et al. 2021), developing tools to aid in their detection and characterization (Izquierdo et al. 2021; Terry et al. 2021). One way to examine these perturbations is by subtracting a best-fitting Keplerian disc model (e.g. Pérez et al. 2018; Teague 2019). After doing-so, the location of a planet may be revealed by a change in sign of velocity residual across a narrow azimuthal section of the disc, known as a Doppler-flip (Pérez et al. 2018; Pinte et al. 2023b). One such Doppler-flip was discovered in HD 100546 by Pérez et al. (2020) and attributed to a $\sim 10 M_J$ planetary companion. However, the signature is also consistent with a more massive companion inside the cavity (Norfolk et al. 2022). If channel maps are inspected, a perturbation in the iso-velocity curve, known as a ‘velocity kink’, may reveal the location of the planet (Perez et al. 2015b; Pinte et al. 2018).

Although there are several convincing indirect detections of planets using the gas kinematics (e.g. Pinte et al. 2018, 2019; Izquierdo et al. 2023), observations also reveal that disc kinematics can be complex (Pinte et al. 2020; Huang et al. 2021). Planets are not the only potential source of perturbations in protoplanetary discs. However, not much attention has been paid to the dynamical effects of other sources. The most well studied is gravitational instability (GI) (Hall et al. 2020; Longarini et al. 2021; Terry et al. 2021; Veronesi

* E-mail: jcalcino@mail.tsinghua.edu.cn

et al. 2021; Lodato et al. 2023), but the conditions for GI are only present in a handful of the most well-studied discs (Paneque-Carreño et al. 2021; Veronesi et al. 2021; Lodato et al. 2023). Expanding our understanding of the dynamical effects that other disc substructure producing mechanisms have on the velocity field of the disc can identify or rule out each mechanism. For example, dust horseshoes could be vortices induced either in planet-hosting (Zhu et al. 2015) or circumbinary discs (Rabago et al. 2023), or they could be overdense lumps in eccentric discs that lack vortical motion (Ragusa et al. 2017; Calcino et al. 2019; Ragusa et al. 2020). Continuum observations alone may not be enough to distinguish between these scenarios. It has been found that the anticyclonic motion inside of a vortex can be detected in the velocity residuals, and appears as a sign change in the velocity residuals across the major axis of the vortex (Huang et al. 2018; Robert, Méheut & Ménard 2020). Boehler et al. (2021) claimed a potential detection of such a signature in HD 142527. However, it is known that this is a binary star system (Billler et al. 2012; Nowak et al. 2024), and it is unclear how the central binary imprints its kinematic signatures on the cavity.

In Calcino et al. (2023, hereafter Paper I), we showcased some of the kinematic features expected to arise in circumbinary discs and developed five criteria to infer binarity. We found three morphological features commonly associated with circumbinary discs: (i) a gas depleted central cavity; (ii) spiral arms inside or outside of the cavity; and (iii) velocity kinks close to the central cavity in the channel maps. We also devised two kinematic criteria which quantify the degree to which the projected velocity field is perturbed. Together, these morphological and kinematic criteria can be used to distinguish circumbinary discs from circumstellar discs under the influence of other effects. In this paper, we expand on these results with a more thorough analysis of the kinematic features seen in circumbinary discs. We study the substructures that arise in the velocity residuals of simulated circumbinary discs. We find striking similarities between our simulations and observations of well-studied transitional discs.

We structure the paper as follows: In Section 2, we briefly present our hydrodynamical simulations and synthetic observations, and introduce the observational data used in this paper. In Section 3, we study the kinematics and residuals of simulated circumbinary discs, identifying fast flows inside the cavity and Doppler-flips as features that can appear. In Section 4, we then demonstrate that these features can explain two examples of kinematic residuals (vortex-like kinematics and Doppler-flips) seen in HD 142527 and HD 100546, and show fast flows are seen inside the cavities of several transition discs. We summarize our findings in Section 5.

2 METHODS AND OBSERVATIONAL DATA

2.1 SPH simulations and synthetic observations

We used the smoothed particle hydrodynamics (SPH; Monaghan 1992) code PHANTOM (Price et al. 2018a). We refer the reader to Paper I for a detailed description of the gas-only SPH models we use in this work; however, we provide a brief description here. A summary of the model parameters is provided in Table 1. Our gas discs are initialized with 5×10^6 SPH particles following a surface density profile $\Sigma(R) \propto R^{-p}$ for $R_{\text{in}} < R < R_{\text{out}}$, where we set $p = 1$ in all models. We assume a locally isothermal equation of state with a temperature profile $T(R) \propto R^{-2q_T}$, and $q_T = 0.25$ in all models. We set the aspect ratio of the disc H/R_{ref} at R_{ref} , with specific values listed in Table 1. The central stars and companions are modelled as sink particles (Bate, Bonnell & Price 1995), where for every simulation, we assume a primary companion mass of $2 M_{\odot}$. The SPH artificial viscosity α_{AV} is used to produce a Shakura & Sunyaev (1973) alpha

viscosity α_{SS} following Lodato & Price (2010), where the value for each model is specified in Table 1. The simulations presented in this work are chosen to reflect a range of binary configurations and disc morphologies without being exhaustive. For example, circular binaries can pump large eccentricities in circumbinary discs, while eccentric binaries can produce comparatively less eccentric discs (Hirsh et al. 2020). Furthermore, circumbinary discs that are coplanar, arbitrarily misaligned (Nowak et al. 2024), or polar aligned (Kennedy et al. 2019), are both theoretically and observationally supported configurations.

Our synthetic observations are the same as shown in Paper I. We used the Monte Carlo radiative transfer code MCFOST (Pinte et al. 2006, 2009). Since our simulations did not include dust, we assumed a power-law grain size distribution $dn/ds \propto s^{-3.5}$ for $0.03 \mu\text{m} \leq s \leq 1 \text{mm}$ with the grains well coupled to the gas. We assumed that $T_{\text{dust}} = T_{\text{gas}}$ and all molecules are at local thermodynamical equilibrium. We only show synthetic ^{12}CO (3–2) line observations in the work and adopted a CO ratio of $^{12}\text{CO}/\text{H}_2 = 10^{-4}$. The CO abundance is affected by photodissociation and freeze out ($T = 20 \text{K}$) (Pinte et al. 2018). Changing the CO line used in our analysis does not significantly alter the kinematic signatures in the velocity residuals we later study. The primary star in each simulation has an effective temperature $T_{\text{eff}} = 8000 \text{K}$ and radius $R = 1.8 R_{\odot}$, giving a blackbody luminosity $\sim 12 L_{\odot}$. The temperature and radius of the companions are computed from their mass listed in Table 1 using the stellar and planetary tracks from Siess, Dufour & Forestini (2000) and Allard et al. (2001). A disc inclination of $i = 30^\circ$, a disc position angle of $\text{PA} = 0^\circ$, and a distance of 100pc were assumed.

The CO cubes from MCFOST were then processed to mimic the finite resolution and sensitivity capabilities of ALMA using the PYTHON package PYMCFOST. The final cubes had a spectral resolution of 250ms^{-1} , and were convolved with a 0.15arcsec Gaussian beam. Artificial noise was added with a flux of $F_{\text{Noise}} = 2.5 \text{mJy}$. Integrated intensity and velocity maps were made from the cubes using BETTERMOMENTS (Teague & Foreman-Mackey 2018) where a cut of $5 \times$ the RMS noise level was applied. We fit the velocity maps using EDDY (Teague 2019). Since the disc flaring is relatively small in our simulations, we fit Keplerian disc models that do not account for the disc flaring. The Keplerian disc models assumed a single central massive body. We did not attempt to fit more complicated rotation profiles (e.g. Ragusa et al. 2024).

2.2 Observational data

We utilized ALMA Band 6 and Band 7 archival ^{12}CO and ^{13}CO line data. The majority of our data was obtained either via private communication as self-calibrated data products, or via the ALMA archive, calibrated using the CASA pipeline for the appropriate ALMA cycle. When selecting our sources, we did not aim to obtain a complete or unbiased sample of discs, as we did not attempt to constrain statistical properties of the disc population. Our sample consists of discs which have been previously studied in other works (e.g. Francis & van der Marel 2020; Wölfer et al. 2023). Our sample is based off the transition disc sampled compiled by Wölfer et al. (2023), excluding sources where the noise levels are too high, or the beam too large, to resolve the kinematics inside the cavity. We also included the MAPS sample (Öberg et al. 2021). In a future work, we will provide a detailed study of the EXOALMA sample. The specific details of the observations are summarized in Table 2. We imaged/re-imaged our data using the *tclean* task in CASA, with the Multiscale Clean deconvolver (Cornwell 2008) with Briggs weighting, and applied JvM (Jorsater & van Moorsel 1995) and primary beam correction. We generated total intensity and velocity maps using

Table 1. A summary of the initial conditions of the models presented in Paper I that are used in this work. Circumbinary disc models are highlighted in bold font. Note that, model OD is taken from Calcino et al. (2019), but the disc parameters have been rescaled.

Ref.	q	a (au)	e	i	ω	$M_{\text{disc}} (M_{\odot})$	H/R_{ref}	R_{ref}	R_{in} (au)	R_{out} (au)	α_{SS}	N_{Orbits}
Planet (P)	2.5×10^{-3}	80	0.0	0.0	0.0	0.010	0.066	100	10	400	5×10^{-3}	60
Multiple planets (MP)	$[2.5, 1.25] \times 10^{-3}$	[75.6, 130]	0.0	0.0	0.0	0.010	0.066	100	10	400	5×10^{-3}	60
Eccentric planet (EP)	2.5×10^{-3}	80	0.4	0.0	0.0	0.010	0.066	100	100	400	5×10^{-3}	60
No overdensity (NOD)	0.25	40	0.0	0	0	0.010	0.066	100	63	400	5×10^{-3}	1100
overdensity (OD)	0.2	30	0.0	0	0	0.005	0.05	45	45	120	1.5×10^{-3}	500
Eccentric companion (EC)	0.1	40	0.4	0	0	0.010	0.066	100	90	400	5×10^{-3}	80
Heavy inclined companion (HIC)	0.25	40	0.5	30	0	0.010	0.066	100	90	400	5×10^{-3}	20
Polar companion (PC)	0.2	40	0.5	90	90	0.010	0.066	100	90	400	5×10^{-3}	60

Table 2. Summary of the observations used in this work. ^(a)Peak SNR refers to the peak signal-to-noise ratio seen in the channels of the cube. ^(b)P/PC: Reimaged data cube. Public data or obtained via private communication, A: Archival data product. HD 163296, MWC 480, GM Aur, IM Lupi, AS 209 (Öberg et al. 2021), HD 9048 (Pinte et al. 2019), HD 169142 (Garg et al. 2022), TW Hya (Teague et al. 2022), GG Tau (Phuong et al. 2020), HD 142527 (Garg et al. 2021), HD 100546 (Law et al. 2022), CQ Tau (Wölfer et al. 2021), AB Aurigae (Speedie et al. in press), J1604 (Stadler et al. 2023), LkCa 15 (this work), CS Cha (Kurtovic et al. 2022).

Object	Line	ALMA project ID	Beam (arcsec)	Δv (km s ⁻¹)	Peak SNR ^(a)	r_{cavity} [arcsec]	Cube source ^(b)
HD 163296	¹² CO (2–1)	2018.1.01055.L	0.15×0.15	0.2	115	–	P/PC
MWC 480	¹² CO (2–1)	2018.1.01055.L	0.15×0.15	0.2	70	–	P/PC
GM Aur	¹² CO (2–1)	2018.1.01055.L	0.15×0.15	0.2	34	0.23	P/PC
IM Lupi	¹² CO (2–1)	2018.1.01055.L	0.15×0.15	0.2	42	–	P/PC
AS 209	¹² CO (2–1)	2018.1.01055.L	0.15×0.15	0.2	69	–	P/PC
HD 97048	¹³ CO (3–2)	2016.1.00826.S	0.11×0.07	0.12	35	0.24	P/PC
HD 169142	¹² CO (2–1)	2015.1.00490.S 2016.1.00344.S	0.073×0.067	0.167	36	0.23	P/PC
TW Hya	¹² CO (2–1)	2013.1.00387.S 2018.A.00021.S	0.19×0.17	0.04	275	–	P/PC
GG Tau	¹² CO (2–1)	2018.1.00532.S	0.34×0.27	0.08	88	1.6	A
HD 142527	¹³ CO (2–1)	2015.1.01353.S	0.35×0.31	0.084	39	1.18	P/PC
HD 100546	¹² CO (2–1)	2016.1.00344.S	0.08×0.06	0.5	29	0.33	P/PC
CQ Tau	¹² CO (2–1)	2013.1.00498.S 2016.A.00026.S 2017.1.01404.S	0.12×0.10	0.5	30	0.36	P/PC
AB Aurigae	¹² CO (2–1)	2021.1.00690.S	0.24×0.17	0.042	86	0.98	P/PC
J1604	¹² CO (2–1)	2018.1.01255.S	0.18×0.15	0.1	84	0.56	P/PC
LkCa 15	¹² CO (3–2)	2018.1.00350.S	0.07×0.05	0.874	50	0.43	P/PC
CS Cha	¹² CO (3–2)	2017.1.00969.S	0.1×0.09	0.25	59	0.25	P/PC

BETTERMOMENTS (Teague & Foreman-Mackey 2018). The total intensity maps were used to obtain the disc radius. We used both the intensity weighted average velocity (Moment 1) and quadratic methods to produce the velocity maps in this paper. When generating our images, we applied noise cuts of $5 \times$ the RMS noise for all cubes.

3 KINEMATIC SIGNATURES IN VELOCITY RESIDUALS

3.1 Doppler-flips

We define a Doppler-flip as a change in sign of velocity across a narrow azimuthal section of the disc (Pinte et al. 2023b). Planet-induced Doppler-flips are produced due to a change in sign of the non-Keplerian gas motion and are centred on the planet (e.g. see Pérez et al. 2018; Bollati et al. 2021; Calcino et al. 2022). Both azimuthal and radial velocities deviations are negative in front of the planet and positive behind it. Since there are both azimuthal and radial velocity perturbations producing the sign-flip, a planet at any azimuthal

position in the disc can produce an observable Doppler-flip. However, since the radial velocity perturbation dominates (Rafikov 2002; Calcino et al. 2022), the Doppler-flip should be stronger along the disc minor axis than along the major axis.

Fig. 1 shows the integrated gas surface density from the circumbinary disc simulations and the velocity residuals from their velocity maps, obtained from ¹²CO (3–2) line emission using the Moment 1 method. We identify similar signatures to planet induced Doppler-flips in the velocity residuals of our models. In contrast to the planet induced Doppler-flips, those seen in circumbinary discs are not centred on the companion and can be a significant distance from it. Supersonic radial and azimuthal velocity perturbations are produced as the companion launches spiral arms and interacts with gas trying to flow inside and fill the cavity. They can also have sudden changes in sign as both the primary and secondary stars launch spiral arms into slower moving material. These large perturbations can persist outside of the gas depleted central cavity and be spatially colocated with the peak in the background gas surface density, which is where we expect large dust grains to accumulate.

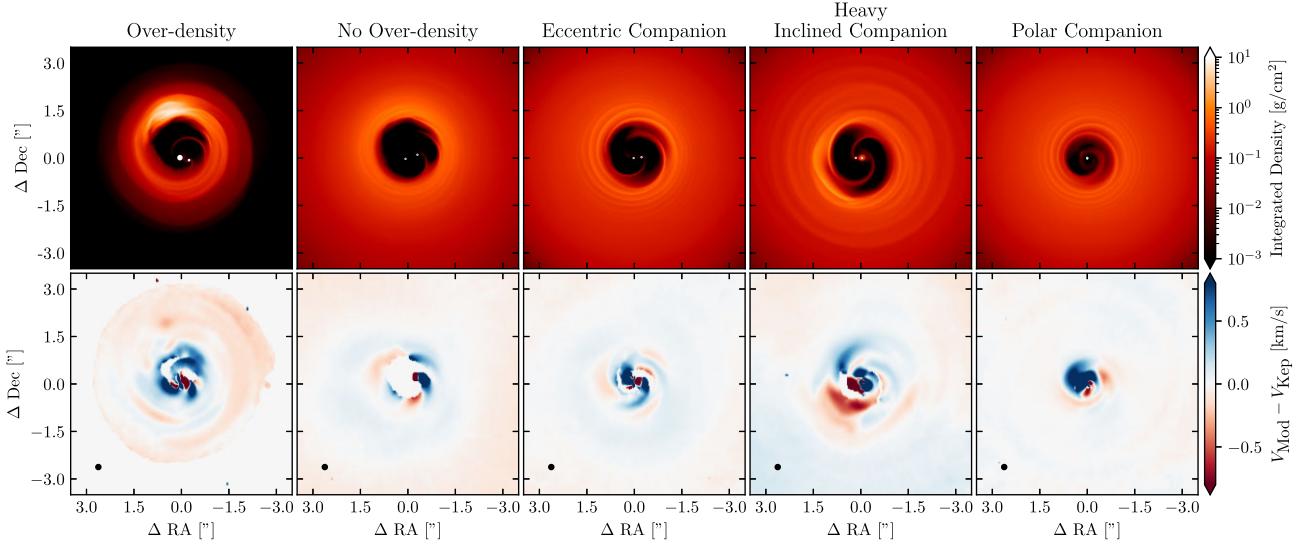


Figure 1. The surface density (top row) with the residuals from Keplerian rotation generated from CO (bottom row) for all our circumbinary disc models. Significant deviations from Keplerian rotation is observed in all models. Spiral arms and Doppler flips are common inside and colocated with the cavity. Since we used a position angle of $PA = 0^\circ$ to produce our synthetic observations, the disc major axis lies along the x -axis. The velocity residuals have been deprojected using our fixed viewing inclination angle of $i = 30^\circ$.

Fig. 2 shows the velocity residuals for our circumbinary disc models at different viewing angles (labelled ϕ). Sudden changes in the sign of the velocity residuals—Doppler-flips—are abundant inside and around the cavity. Arrows in Fig. 2 indicate several prominent Doppler-flips. We also mark the approximate radial location of the gas pressure maximum around the cavity with a dot–dash circle. The location of the Doppler-flips relative to the cavity also suggests that they could be colocated with other features attributed to circumbinary discs, such as dust rings or dust asymmetries. Whether or not a Doppler-flip is seen can depend on the disc model that is subtracted. In Fig. 4, we show the velocity residuals of model OD with three different Keplerian models which were obtained by changing the minimum radius, r_{\min} , that is used in the fit with EDDY. The disc model in EDDY assumes the gas is on a circular Keplerian orbit around a single star. Although the high amplitude Doppler-flips (shown with an arrow in all three columns) do not change sign, lower amplitude residuals, particularly in the outer disc (bottom right of right-most panel), can change sign. In principle, this is not just an issue when fitting the velocity map of known circumbinary discs, but also for single stars (e.g. Teague et al. 2022). By their very definition, velocity residuals are model dependent, and the appearance of a Doppler-flip is therefore also model dependent. However, high amplitude Doppler-flips are less dependent on the Keplerian model that is subtracted, as shown in Fig. 4.

These results demonstrate that the appearance of Doppler-flips, particularly low velocity (i.e. order few hundred metres per second) are sensitive to the disc model that is subtracted. Since we assume a Keplerian background model, large residuals should be expected. However, what is notable is that the large residuals can still be visible in proximity to the cavity edge and gas pressure maxima. For example, in the HIC model (fourth row, first column of Fig. 2), a Doppler-flip on the order of several hundred metres per second is seen just interior to the gas pressure maxima at a radial location exterior to the binary orbit.

The Doppler-flips we observe in our simulations are also sensitive to the CO isotopologue they are observed with, as shown in Fig. 3. In fig. 9 of Paper I, using the same simulation we use here, we showed how velocity kinks seen in the channel maps also depend on

the CO isotopologue. In that Figure, the apparent amplitude of the kink decreases due to the more highly perturbed material responsible for the kink becomes unobservable due to the lower abundance. The same effect results in the Doppler-flips becoming less apparent in the residual maps of Fig. 3.

The ubiquity of Doppler-flip features in a circumbinary disc suggests that they should not be used as an indicator of planet-disc interactions, particularly when they are in proximity of a gas and dust depleted cavity in a transition disc. Contrary to those generated by planets, Doppler-flips in CBDs are not necessarily directly associated with a companion, but rather, they are a result of spiral structure exterior to the binary orbit. The structure of the Doppler-flips we observe are reminiscent of the one in HD 100546 reported by Casassus & Pérez (2019), which we comment more on in Section 4.2.

3.2 Spiral arms: the origin of Doppler-flips

Circumbinary discs are rich with spiral structure. These spirals are visible in the velocity residuals. Planet-induced Lindblad spirals appear mostly as radial perturbations and the radial velocity changes sign across the spiral (Bollati et al. 2021; Calcino et al. 2022). The spiral arms induced by stellar mass companions produce larger perturbations in the velocity field of the gas than their planetary counterparts, although they are still mostly generated by Lindblad resonances. The spiral structure is most abundant near and inside the cavity. Since this area is also typically associated with (sub-)mm dust continuum emission, spiral structures may also be imprinted on the dust continuum emission. Planet induced spiral wakes are visible in the mm dust continuum emission if the dust and gas are well coupled (e.g. Speedie, Booth & Dong 2022; Verrios et al. 2022). Poblete, Cuello & Cuadra (2019) showed that marginally decoupled dust grains can produce dusty clumps around the central cavity. It is plausible that the binary induced spiral structure may be imprinted in the mm dust continuum if the grains are sufficiently coupled to the gas.

In Paper I, we showed that spiral structure in and around the central cavity of a CBD produces substantial velocity perturbations away from Keplerian rotation. These perturbations are manifested as large

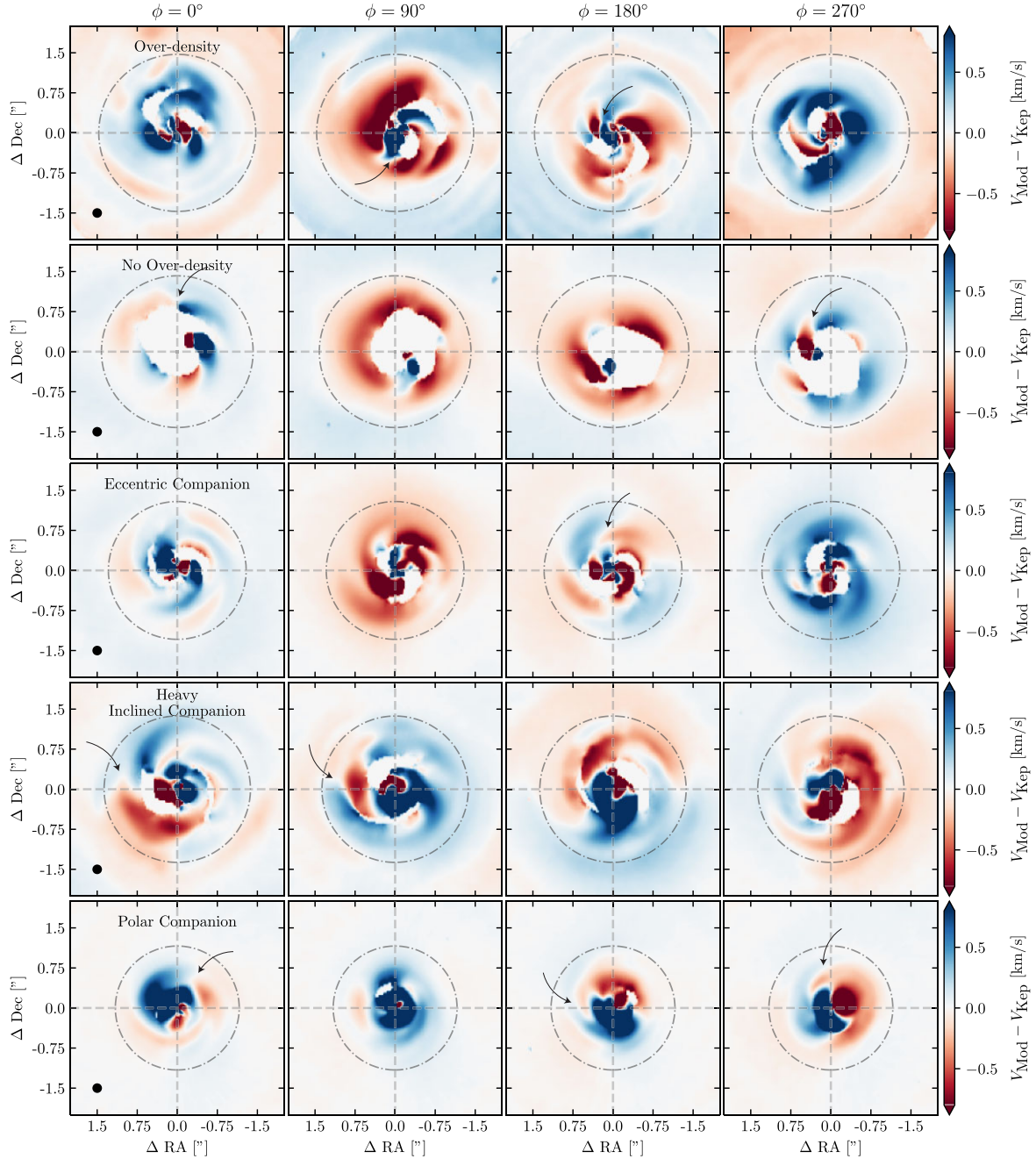


Figure 2. Binaries produce Doppler flips: Deprojected residuals from Keplerian rotation obtained using EDDY for all circumbinary models listed in Table 1 for four different viewing angles (left to right columns). The horizontal and vertical grid lines (left to right columns) are along the major and minor axis of the disc, respectively. The dash-dot circle shows the approximate radius of the cavity, obtained from the peak in the azimuthally averaged gas surface density. Doppler flips and spiral arms are ubiquitous in and around the cavity. Several prominent Doppler flips are marked with arrows.

residuals after subtracting the best-fitting Keplerian disc model, and occasionally produce the Doppler-flips we discussed in the previous section. Given the causal link between spiral arms and Doppler-flips, we should then expect that a Doppler-flip observed on the edge of a cavity, produced by an inner binary, should be accompanied by spiral structure.

Spiral structure not only originates directly from the binary interacting with the disc through Lindblad resonances, but also from the overdensity that can develop. In the left most column of Fig. 5, we show our model with an overdensity (model OD) in integrated surface density with the corresponding velocity residuals

below. The overdensity is highlighted by white and black dashed lines in the surface density and velocity residuals, respectively. There is additional spiral structure through the disc that is not seen in the no overdensity (NOD) model, shown in the right column, which has a very similar cavity size and shape as model OD. The formation of the overdensity is likely related to the growth of the eccentric cavity, where a disc initialized with a smaller cavity leads to a more prominent overdensity developing (see section 4.3 of Ragusa et al. 2020, for more details). Thus, the spirals are a direct result of the overdensity, and not due to the eccentric cavity. These spirals propagate far from the cavity, and are also apparent in the velocity

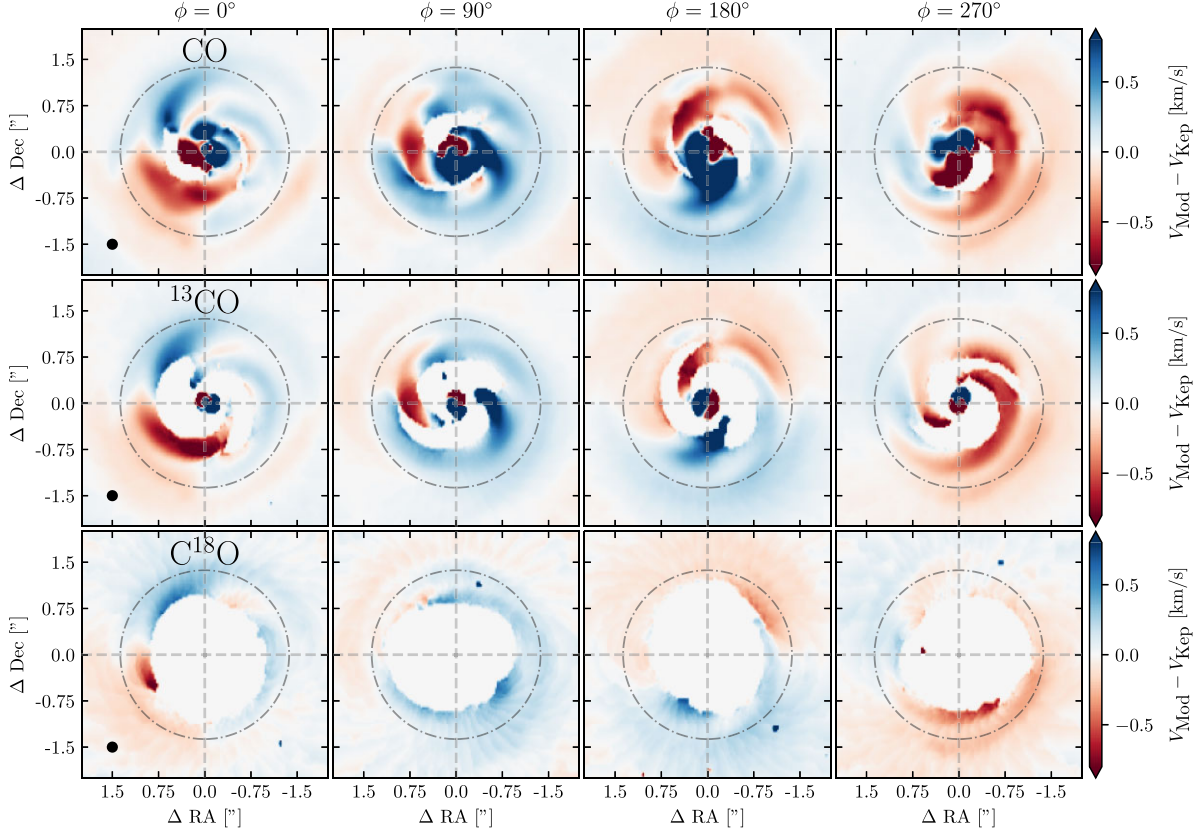


Figure 3. Deprojected residuals from Keplerian rotation obtained from the velocity map constructed from ^{12}CO (3–2) (top row), ^{13}CO (3–2) (middle row), and C^{18}O (3–2) lines. Each column is the same simulation but seen from a different viewing angle.

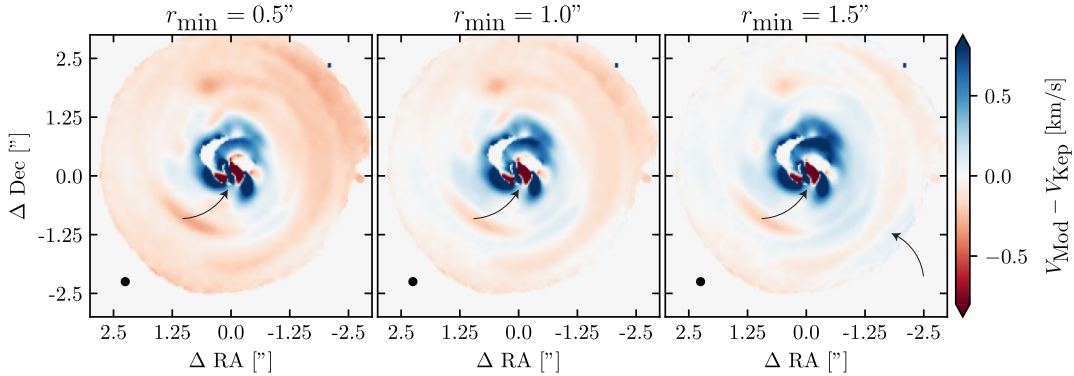


Figure 4. The deprojected residuals from Keplerian rotation for model OD with $\phi = 0^\circ$ with three different values of the inner radius for the fitting with EDDY. The residuals can change sign depending on the background model that is subtracted. The large amplitude residuals in the inner regions are not sensitive to the model subtracted, while the lower amplitude residuals in the outer disc are.

residuals. Since our model does not include gas self-gravity, the spiral structure produced from the overdensity is not due to the gravitational potential of the overdensity exciting spiral wakes (e.g. see Zhu & Baruteau 2016). We note that a similar trailing spiral is seen in the CBD simulations of Rabago et al. (2023). The spiral from the overdensity is generated by hydrodynamical effects: the overdensity is a localized region of higher density and pressure which perturbs the surrounding disc material as it orbits, resulting in the additional spiral structures. We show in Section 4.1 that the overdensity might be responsible for the extended spiral structure seen in HD 142527.

3.3 Eccentric cavity

In three of our models, the gas orbiting around the cavity has a non-negligible eccentricity which appears in the velocity residuals. These are models overdensity (OD), no overdensity (NOD), and eccentric companion (EC). Large red and blueshifted residuals become more apparent when the eccentricity vector of the disc is pointing perpendicular to the line of sight, which is the case when $\phi = 90^\circ$ and $\phi = 270^\circ$ in Fig. 2.

The residuals from eccentric discs arise due to the sub and super-Keplerian motion that occur at apoapsis and periapsis, respectively.

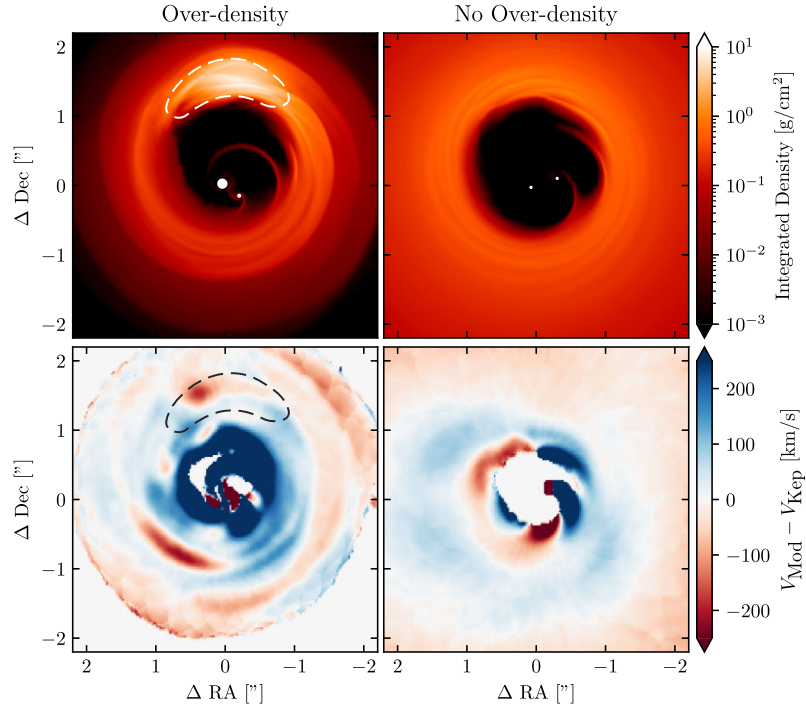


Figure 5. The surface density (top row) with deprojected residuals from Keplerian rotation generated from CO (bottom row) of models overdensity (OD), and no overdensity (NOD). The overdensity produces a Doppler-flip signature across its major axis. There is also additional spiral structure through the disc with OD than in no OD model, which has a very similar cavity size and shape as model OD. These additional spirals are arising due to the overdensity feature, and are apparent in the velocity residuals.

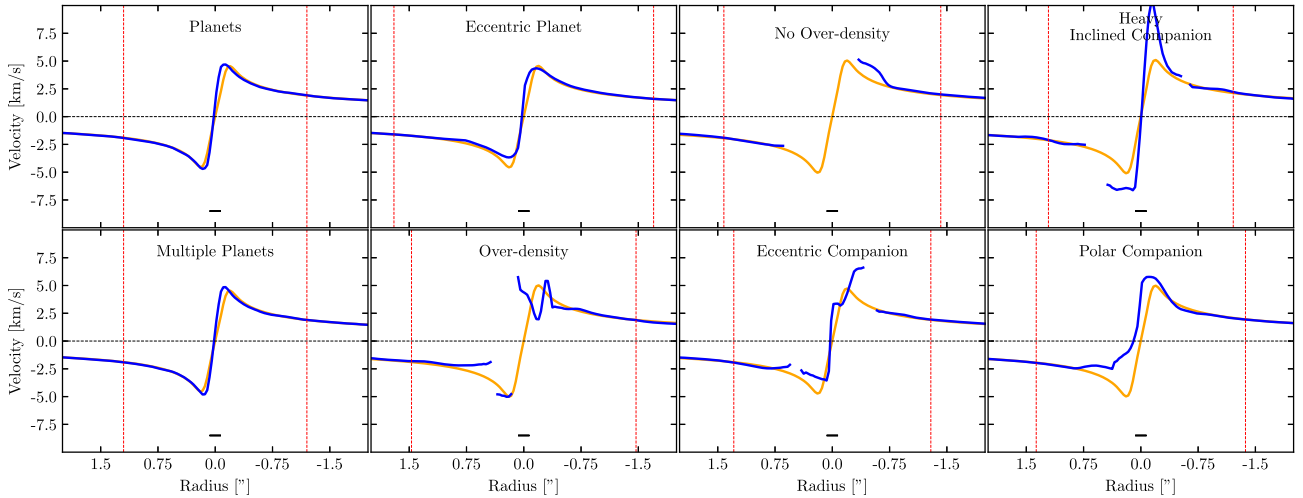


Figure 6. The rotation curve along the disc major axis of each model presented in Table 1 (dark lines) with the expected Keplerian rotation of the unperturbed disc (light lines). The vertical red lines mark the location of the edge of the cavity as seen with C¹⁸O (fig. 5 of Paper I). Minor deviations from Keplerian rotation are seen in the Planet and Multiple Planets models, mostly due to the assumptions used to generate the Keplerian rotation curve. Modest deviations from Keplerian rotation are seen inside the cavity of the Eccentric Planet model, while in most of the circumbinary disc models several km s⁻¹ deviations are seen. Since radial velocities are largely perpendicular to the line of sight along the major axis, the deviations from Keplerian rotation are mostly due to azimuthal perturbations. The black horizontal line represents the size of the beam major axis.

When fitting a velocity map it is common to mask the central regions (e.g. Teague et al. 2021, 2022). For a disc with a cavity and substantial deviations from Keplerian rotation, these non-Keplerian motions are also often masked out (e.g. Boehler et al. 2021; Wölfer et al. 2021; Norfolk et al. 2022). As we show in Fig. 4, the final residual map that is obtained depends on the model that is subtracted, which in our eccentric disc models is sensitive to the minimum radius assumed. This issue could be alleviated by fitting an eccentric disc rotation

profile to the observations (e.g. Kuo et al. 2022; Yang et al. 2023). For a circumbinary disc, we expect that the disc eccentricity decreases as a function of disc radius, and hence only the regions close to the cavity may be highly eccentric.

Aside from the kinematics (Kuo et al. 2022), an eccentric cavity might also be inferred from the spatially resolved distribution of gas (through line emission observations) and dust (through scattered light or thermal emission observations; Dong et al. 2018a; Yang

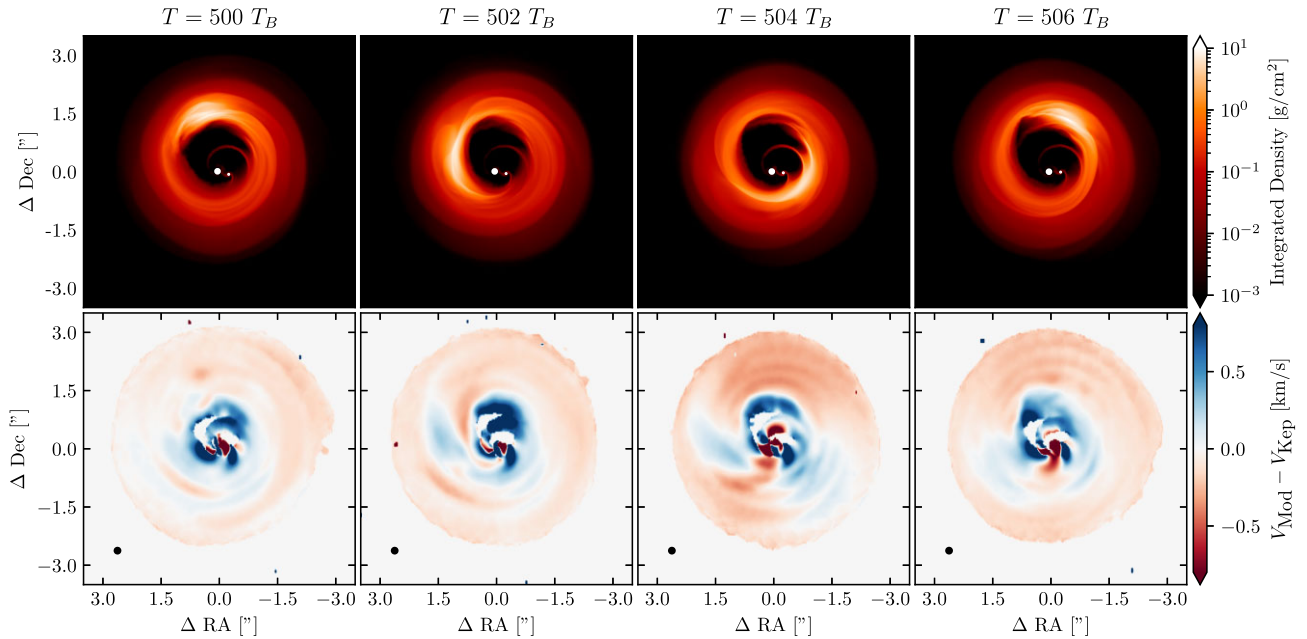


Figure 7. The surface density (top row) moment 1 (top row) with deprojected residuals from Keplerian rotation generated from CO for model OD at different time snapshots. Significant deviations from Keplerian rotation is observed in all models. Spiral arms and Doppler flips are common inside and colocated with the cavity.

et al. 2023). If the location of the primary star can be determined, deprojecting the spatially resolved observations can also lead to constraints on the disc eccentricity (Yang et al. 2023).

3.4 Fast flows inside the cavity

As we showed in Paper I, and in Fig. 1, both radial and azimuthal velocity perturbations increase inside the cavity of a circumbinary disc. For the inclined companion models, non-negligible vertical motion is also observed. After subtracting a best-fitting Keplerian rotation field, these fast flows are obvious in the residuals (Fig. 1) and span the entire width of the cavity. In some instances, the residuals change sign across the major axis of the disc (e.g. first column of model NOD in Fig. 2), indicating mostly radial flows (e.g. Teague, Bae & Bergin 2019) (e.g. model HIC), while in other instances, a superposition of azimuthal and radial velocities lead to no obvious sign change across either the major or minor axes (e.g. multiple viewing angles of models OD and NOD).

To further explore how these fast flows appear in observations, Fig. 6 shows the velocity along the major axis of the disc neglecting any disc flaring with the blue curves, while the orange curves show the expected mid-plane Keplerian rotation neglecting any disc flaring and gas pressure support. Along the major axis, the radial velocity component of a disc is negligible since the major velocity component is perpendicular to the line of sight. For the planet simulations (model P and MP), the deviations from the estimated Keplerian rotation are small. In contrast, the eccentric planet model and the circumbinary disc models show larger deviations. These perturbations span several beams and hence are not localized. They also exceed estimates of the local sound speed by a factor of several. Highly perturbed rotation curves inside of a cavity can thus indicate that the disc is circumbinary. Similar perturbations are seen in the rotation curve and residuals inside the cavity of GG Tau and AB Aurigae (Rivière-Marichalar et al. 2019; see also Section 4.3).

3.5 Vortex-like kinematic signatures

Fig. 7 shows the surface density and velocity residuals of the overdensity model for four different snapshots which trace the orbital phase of the overdensity. The overdense feature arises as the eccentric cavity grows around the binary (Ragusa et al. 2020), and is distinct from a vortex as it lacks vortical motion (Ragusa et al. 2017). Since it orbits around the cavity at the Keplerian frequency, it is also not a ‘traffic-jam’ of dust grains at the apocentre of an eccentric disc (Ataiee et al. 2013). In Paper I, we showed that the overdense feature orbiting a circumbinary disc also shows a change in velocity across the major axis of the overdensity. Since the residuals are dominated by excess velocities arising from the eccentric gas motion around the cavity, the signature from the overdense feature can be difficult to distinguish.

In left column of Fig. 5, we see that this change in velocity is apparent in the velocity residual. The overdensity is outlined with a dashed line in the integrated surface density and velocity residual plots. A change in sign across the major axis of the overdensity is apparent. The inner binary clearly complicates any analysis of the kinematics. This fact demonstrates that even with high spectral and spatial resolution observations, disentangling the velocity signature of the overdense feature, or ‘vortex’ as in Boehler et al. (2021), is difficult.

4 APPLICATIONS TO OBSERVED KINEMATIC FEATURES

4.1 HD 142527

HD 142527 is a well studied binary system containing a 0.1–0.4 M_{\odot} companion (Biller et al. 2012; Close et al. 2014; Lacour et al. 2016; Christiaens et al. 2018). It also displays non-Keplerian gas flows (Casassus et al. 2015; Garg et al. 2021) inside of its ~ 140 au cavity (Casassus et al. 2013; Avenhaus et al. 2017).

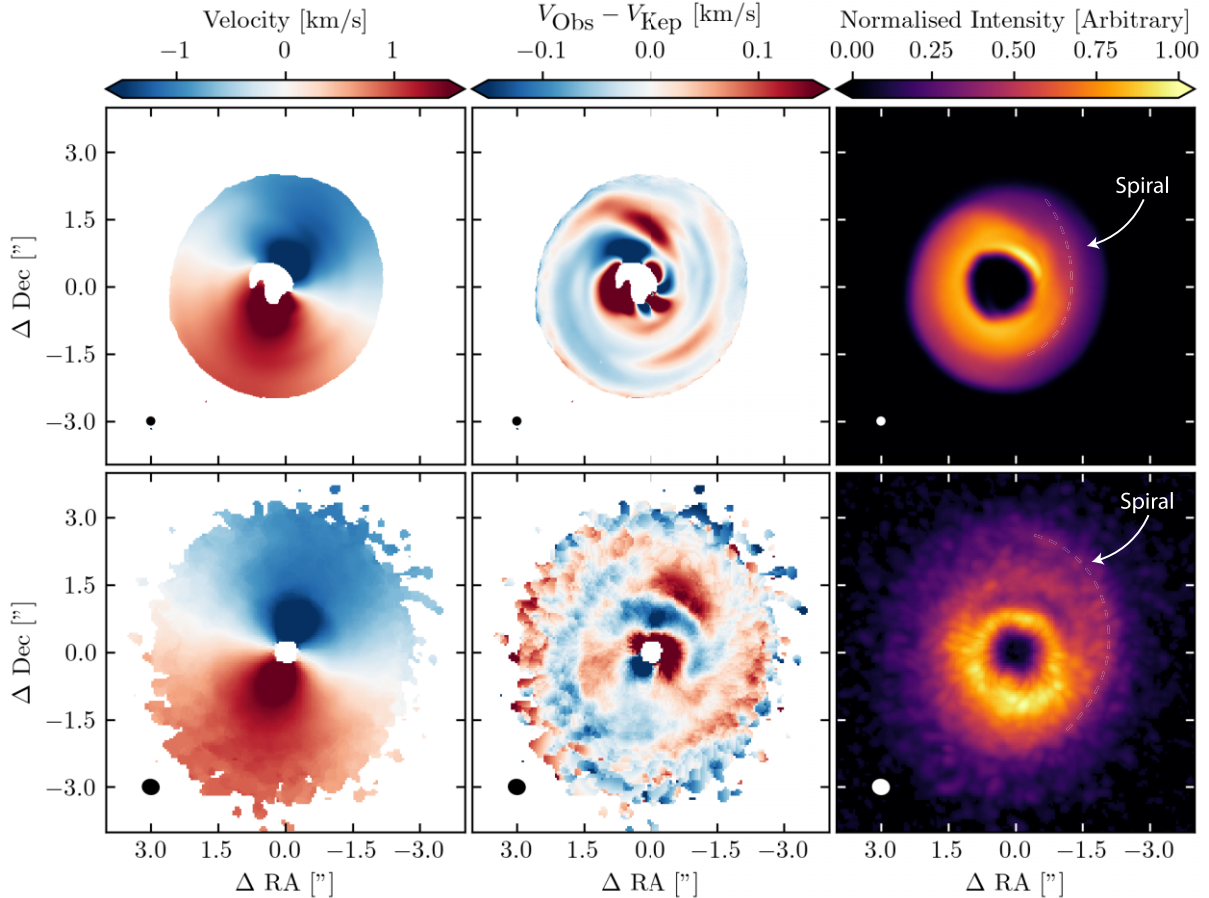


Figure 8. The moment 1 (left column), moment 1 residuals from a best-fitting Keplerian disc model (middle column), and the peak intensity (right column) of our overdensity model (top row), and HD 142527 (bottom row). The overdense feature can reproduce the spiral structure seen in HD 142527 in both peak intensity and in the velocity residuals. The location of the overdense feature is similar in both the model and observations. A Doppler flip across the overdensity is reproduced in our model.

This binary was subject to the study by Price et al. (2018b), where it was shown that many of the morphological features in this disc can be explained by the observed companion, assuming a rather large binary semi-major axis of $\sim 30\text{--}40$ au. Recently, Nowak et al. (2024) constrained the semi-major axis of HD 142527B to ≈ 10 au, which is too small to completely explain the observed cavity size. Nevertheless, spiral arms have been observed in the outer disc in CO integrated emission and peak intensity (Christiaens et al. 2014; Garg et al. 2021). They are also seen after subtraction of a best-fitting Keplerian disc model by Boehler et al. (2021), along with kinematic signatures hypothesized to originate from anticyclonic motion (which we refer to as ‘vortical motion’) inside the dust trap (Ohashi 2008; Casassus et al. 2013). We have shown that such kinematic features can also be seen in a circumbinary overdensity, and may explain both this feature and the spiral arms.

To demonstrate this, we rescale our model OD such that the primary star has a mass of $1.8 M_{\odot}$, consistent with the mass of HD 142527 (Fukagawa et al. 2006). The length is rescaled by a factor of 3.8 from the original model presented in Calcino et al. (2019) such that the total diameter of the cavity along the major axis is ~ 280 au. When performing our radiative transfer calculations we closely follow the prescription summarized in Section 2.1 with a few differences. We set the inclination to $i = 27^{\circ}$ and position angle $\text{PA} = -20^{\circ}$ (Avenhaus et al. 2014; Perez et al. 2015a). The

temperature and radius of the central star are set to 6500 K and $2.8 R_{\odot}$ (Mendigutía et al. 2014). For the companion, we assume a temperature of 3000 K and radius of $0.9 R_{\odot}$ (Lacour et al. 2016). We also scale the total gas mass of our simulation to be consistent with the gas surface density estimates from Garg et al. (2021).

We obtained the ALMA ^{13}CO data (2015.1.01353.S, PI Christiaens) used in Garg et al. (2021) and Boehler et al. (2021). We show the velocity map, velocity map residuals, and ^{13}CO peak intensity of this data and our model in Fig. 8. First, we see that our model recreates the observed spiral arms in the outer region of the disc found by Christiaens et al. 2014 and further studied by Garg et al. 2021. These spirals are associated with perturbations in the velocity field of the disc (see figs 1 and 4 in Paper I) and appear in our velocity residuals. These are also seen in the data of HD 142527, as reported by Boehler et al. (2021). Our model is also able to recreate the Doppler-flip colocated with the overdensity. Boehler et al. (2021) suggest that this feature is arising due to vortical motion inside the dust trap in HD 142527; however, our results show that such a feature can be created without any vortical motion. Indeed, while analysing our model, we found that Doppler-flips close to the cavity edge are exceptionally common, with some colocated with the overdensity while others are not. This should not be too surprising given the complex kinematics seen in our simulations in figs 1 and 3 of Paper I.

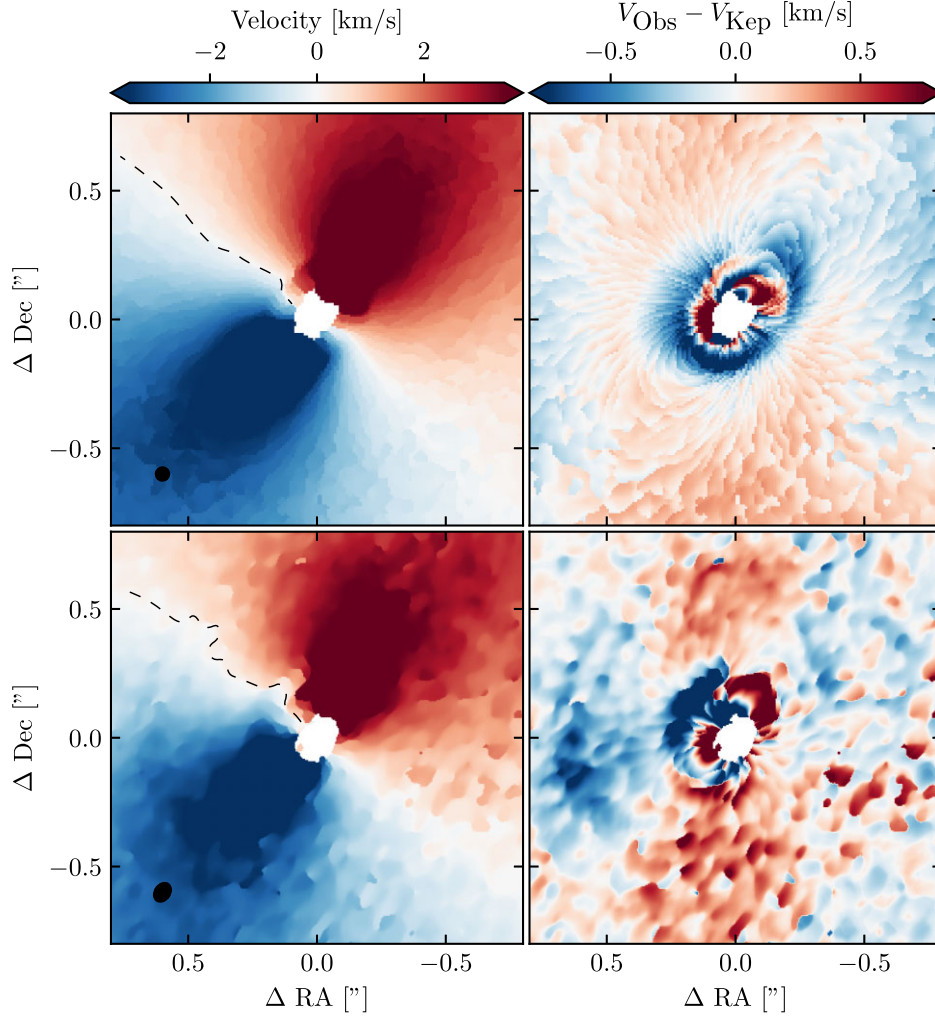


Figure 9. The velocity map produced with the quadratic method (left column) and the residuals from a best-fitting rotation profile (right column) of our eccentric disc model (top row) and HD 100546 (bottom row). Our eccentric disc model reproduces the kink in the velocity map and the excess in velocity residuals around the cavity of the observations. We produce the Doppler flip signature with our eccentric companion model.

Recently, Rabago et al. (2023) studied misaligned circumbinary discs using the grid code ATHENA++ , allowing them to have fine control over the disc viscosity. Most previous studies employ smoothed particle hydrodynamics (e.g. Price et al. 2018b), where it is more difficult to study circumbinary discs with low ($\alpha < 10^{-4}$) viscosity. The results from Rabago et al. (2023) mostly agree with previous SPH results regarding disc breaking, warping, and cavity size. Interestingly, in their $\alpha = 10^{-5}$ simulation, a long-lived vortex is formed in the circumbinary disc. The anticyclonic motion inside the vortex is distinct from the mostly solid-body motion of the lump seen in SPH simulations. However, it is unclear whether it would be possible to distinguish between these two scenarios using disc kinematics alone as the velocity residuals of a circumbinary disc are already complicated. We note that the simulations by Rabago et al. (2023) also cannot explain the observed cavity size given the ~ 10 au semi-major axis of HD 142527B. A low disc viscosity alone cannot explain the large cavity size. Another companion inside the cavity, or including additional physics in the simulation, may resolve this issue.

We summarize that the spiral arms in CO integrated emission and peak intensity, along with their associated kinematic signatures, may directly arise from the horseshoe feature in HD 142527. It is unclear

whether the kinematics of the horseshoe feature can be interpreted as a vortex in a circumbinary disc, as they are also consistent with an overdense feature lacking vortical motion. In light of the recent results of Nowak et al. (2024), it is not clear if there is a direct causal link between the dust overdensity and the inner binary in HD 142527.

4.2 HD 100546

The Herbig Ae/Be star HD 100546 is surrounded by a transition disc which displays all of the morphological features we can attribute to a circumbinary disc. First, it displays a cavity of radius ~ 20 au in the \sim mm dust continuum which extends out to ~ 40 au (Wright et al. 2015; Pineda et al. 2019; Pérez et al. 2020; Norfolk et al. 2021), with a faint ring located at 200 au (Walsh et al. 2014; Fedele et al. 2021). The most central dust continuum ring also shows an asymmetry, which in the higher resolution observations of Pérez et al. (2020) resemble tightly wound spiral arms. A cavity is also present in the ^{12}CO , implying it is heavily depleted in not just large dust grains, but also gas (Pineda et al. 2019; Pérez et al. 2020). Spiral arms are also observed in scattered light close to the cavity and on larger scales at the edge of the protoplanetary disc (Sissa et al. 2018; Fedele et al. 2021). Finally, velocity kinks are seen in the ^{12}CO iso-velocity curves

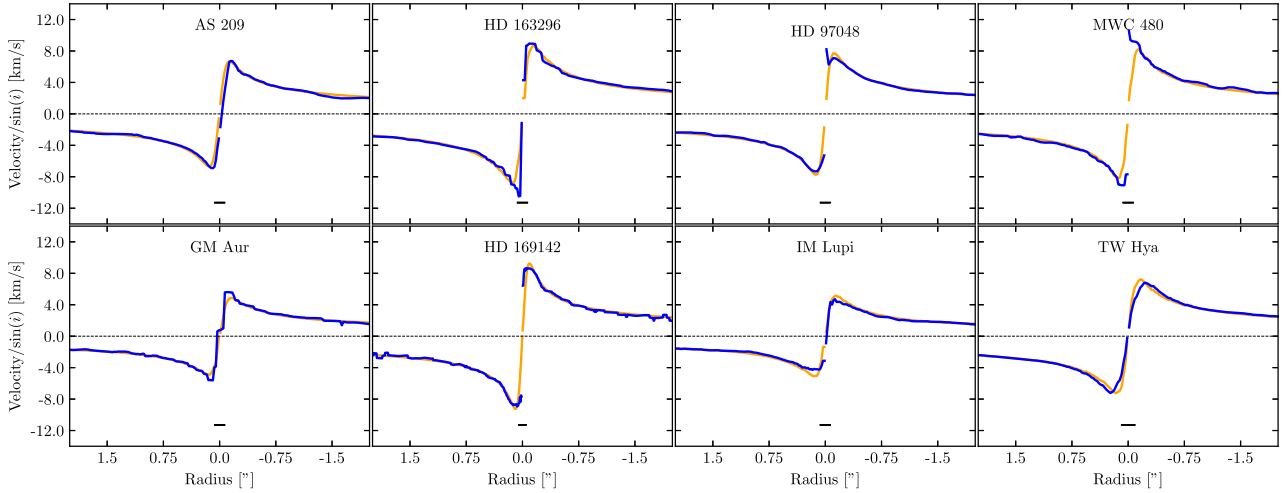


Figure 10. The rotation curve along the disc major axis of the first 8 observations listed in Table 2 (dark lines) with the expected Keplerian rotation of the unperturbed disc (light lines). For the HD 163296, GM Aur, IM Lupi, and MWC 480, we have taken the elevated emission surface into account in the Keplerian rotation model. The major axis of the beam is shown as the horizontal black line. Most of the discs in this Figure show few deviations away from the expected Keplerian rotation. Where such deviations do exist, they tend to be within one or two beam sizes from the centre of the disc, where the rotation profile of the disc is unresolved. IM Lupi shows some larger deviations; however, this is likely due to uncertainties in modelling the highly elevated emitting layer, and its observational effects. TW Hya shows modest deviations away from the Keplerian model that appear several times larger than the beam, but these may be due to the dust continuum subtraction process.

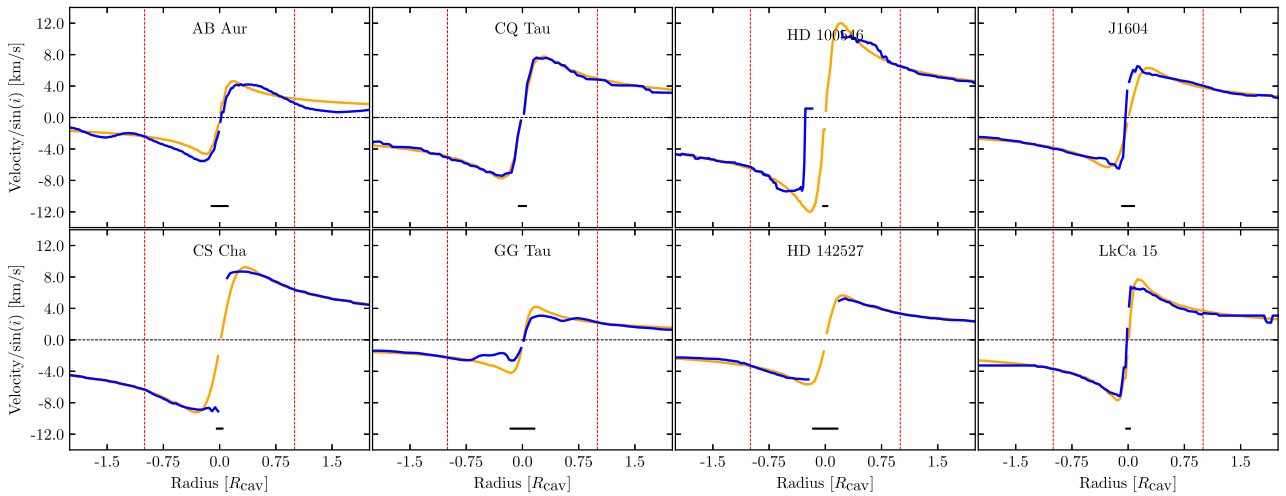


Figure 11. As in Fig. 10 but for the last 8 discs listed in Table 2. CS Cha, GG Tau, and HD 142527 are confirmed circumbinary(-triple) discs. While all three of these discs so show some perturbations away from Keplerian, they are most obvious in GG Tau. The optically thin ^{13}CO and ^{12}CO cavities inside of HD 142527 and CS Cha limit our ability to spatially resolve their gas kinematics. Modest perturbations are also seen inside the cavities of J1604 and LkCa 15.

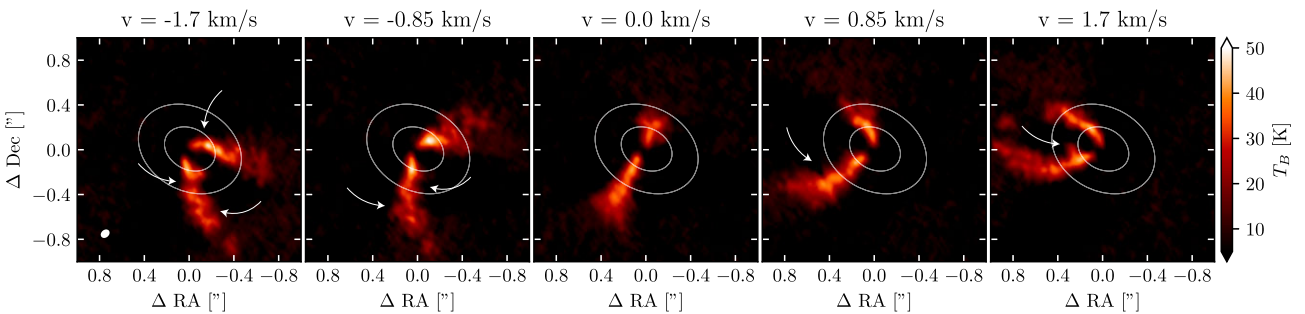


Figure 12. The CO (3–2) emission around LkCa 15. The white ellipses mark the inner and outer extent of the two bright continuum emission rings (Facchini et al. 2020). Kinks in the iso-velocity curves are seen inside and in proximity to the continuum emission, and are marked with the white arrows.

outside of and on the edge of the cavity (Pérez et al. 2020), along with a Doppler-flip on top of the \sim mm continuum ring (Casassus & Pérez 2019). Kinematic perturbations are also observed inside the cavity around the \sim mm continuum emission associated with the central star (Pérez et al. 2020). Casassus & Pérez (2019) and Pérez et al. (2020) attributed these kinematic signatures to a 5–10 M_J planet, and suggested the Doppler-flip on top of the continuum emission results from gas flows close to the planet. This scenario is in tension with the position of the continuum emission; such a large planet will carve a gap and produce a pressure maximum beyond its orbital location. Dust grains will accumulate inside this pressure maximum and thus we should reasonably expect a Doppler-flip signature to be seen well inside the dust cavity, and not on top of the dust continuum emission.

fig. 1 of Casassus & Pérez (2019) shows the deprojected continuum emission with the Doppler-flip superimposed. From this perspective, the Doppler-flip looks to be associated with the spiral structures in the continuum ring. Several of our circumbinary disc models do show sharp changes in gas velocity associated with spiral arms on the cavity edge, potentially explaining this feature in HD 100546. To demonstrate this, we obtained the CO $J = 2-1$ from Pérez et al. (2020), made publicly available from Law et al. (2022). We also reproduced our eccentric companion model with a new simulation with a binary semi-major of 10 au, and eccentricity of 0.4. We produced synthetic CO $J = 2-1$ observations assuming stellar parameters similar to those in HD 100546 ($T = 9750$ K, $M_* = 2 M_\odot$; Vioque et al. 2018).

We produce velocity maps using the quadratic method (Teague et al. 2018) and compute their residuals using EDDY. These are shown in Fig. 9 for our model (top row) and the observations (bottom row). As indicated by the dashed black line, which marks the $v_{\text{los}} = 0 \text{ km s}^{-1}$ iso-velocity curve, the velocity kink seen in the channel maps (see Pérez et al. 2020; Norfolk et al. 2022) also appears in the velocity map. Aside from the Doppler-flip reported by Pérez et al. (2020), there also appear to be other significant velocity perturbations further inside the dust cavity. The Doppler-flip signature along with the other perturbations inside the cavity are reproduced in our eccentric companion model.

Recently Casassus et al. (2022) proposed that the Doppler-flip signal in HD 100546 could be due to a disc eruption event or inflow onto the disc. The latter hypothesis seems rather unlikely, as it is not clear how inflowing material could produce both blue and redshifted emission. The disc eruption scenario also lacks a physical mechanism to explain the eruption, and whether such a scenario could produce both blue and redshifted super-sonic perturbations that span roughly half the azimuthal extent of the disc (and appear inside of the cavity) is not demonstrated. The association of a Doppler-flip with spiral structure seen in the continuum emission (Casassus et al. 2022), as well as emission from the shock tracing molecule SO (Booth et al. 2018, 2023), is expected with our scenario of a massive internal companion.

The main criticism of our proposal is that such a companion probably should have been detected in the sparse aperture masking observations with VLT/SPHERE by Pérez et al. (2020), and more recently by Stolker et al. (2023). However, as noted in Norfolk et al. (2022), the observations by Pérez et al. (2020) conducted in 2018 May, and more recently throughout 2021 and 2022 by Stolker et al. 2023, were conducted when a suspected companion detected by Brittain et al. (2014) was predicted to be behind the near-side of the disc (Brittain, Najita & Carr 2019). Interestingly, Stolker et al. (2023) find a bright spot on the near-side of the disc that is in close proximity to where one would expect this potential companion to be located. However, they conclude that this bright spot is due to bright

forward scattering on the near-side of the disc. Additional sparse aperture masking observations tracking these bright spots may help to constrain their orbital motion and determine if either are consistent with predictions made by Brittain et al. (2014, 2019).

4.3 Fast-flows inside the cavities of transition discs

We show the velocity close to the disc major axis of the first 8 discs of Table 2 in Fig. 10, and the last 8 discs of Table 2 in Fig. 11. The observed velocities are taken assuming either an elevated emission surface (for GM Aur, HD 163296, IM Lupi, and MWC 480, where the emission surfaces are taken from Law et al. 2021) or pure Keplerian rotation (all other observations). We fit each velocity map with EDDY and use the resulting best-fitting Keplerian model 2D velocity map to obtain the velocities along the same path close to the disc major axis as the observations. In both figures, we scale the line-of-sight velocity by $\sin(i)$, where i is the inclination of the system. The observations are shown with the blue lines, while the models are shown with the orange lines.

Starting with Fig. 10, we notice that close to the central regions of the disc, there can be large deviations from the best-fitting model. Smearing of the high-velocity components close to the central regions, along with uncertainties in the height of the emitting layer, can cause these effects. We note that these perturbations tend to be about one or two beam sizes in extent. Larger-scale perturbations are seen in IM Lupi and TW Hya. In IM Lupi, the deviations are likely originating due to the CO emitting layer and disc inclination producing a complex CO emission line profile that is not taken into account in our model. TW Hya appears to have kinematic perturbations that are several beam widths across which may be due to continuum subtraction process (e.g. see Boehler et al. 2021).

Turning our attention to Fig. 11, we note that the x -axis has been rescaled to the size of the cavity for each of the discs, as listed in Table 2. Several discs presented are confirmed circumbinary (or -triple) discs. These are GG Tau (Leinert et al. 1993), HD 142527 (Biller et al. 2012), and CS Cha (Guenther et al. 2007; Nguyen et al. 2012). Starting with GG Tau, CO emission is seen within the cavity region, allowing for the highly perturbed kinematics to be traced (Phuong et al. 2020). Significant deviations from the best-fitting Keplerian rotation curve are seen, which are consistent with the perturbations we see in our models in Fig. 6. Deviations from Keplerian rotation are also seen in the rotation profiles of CS Cha and HD 142527, but since CO emission is missing inside of the cavity, larger perturbations are not seen.

Two other discs stand out as having large perturbations inside of their cavities: AB Aur and HD 100546. AB Aur has a claimed detection of a companion by Currie et al. (2022), and their astrometric fitting suggests it is highly eccentric and inclined with respect to the disc. Such a body could lead to significant perturbations inside the cavity, larger than those suggested by our planet-hosting disc models in Paper I. However, it is not clear whether this detection is a feature on the disc surface or truly an embedded protoplanet (Zhou et al. 2023; Biddle et al. 2024, however, see Currie 2024). The outer disc appears to be highly perturbed, and potentially gravitationally unstable (Speedie et al., in press), which may be responsible for the perturbations in this region. But the central cavity is optically thin in ^{13}CO (Rivière-Marichalar et al. 2020), possibly ruling out GI as the primary source of perturbations in this region.

HD 100546 has had several claimed detections of protoplanets, both inside (Currie et al. 2015) and outside (Quanz et al. 2013) the central cavity. Fig. 6 shows that planetary mass companions do not produce large amplitude perturbations inside of the cavities

they generate. The highly perturbed kinematics inside of the cavity are suggestive of a more massive companion generating the central cavity and the other observed morphological features seen in this disc.

Modest perturbations are also seen in both J1604 and LkCa 15. For J1604, it is not entirely clear whether these perturbations are rotational or out of the plane of the disc (Stadler et al. 2023). It is feasible that either a planetary mass companion on a non-circular orbit, or a more massive companion, can produce such perturbations (see Fig. 7). In LkCa 15, the relatively low signal-to-noise, sparse spectral resolution, and relatively large disc flaring, make interpreting the perturbed kinematics difficult. However, the channel maps, shown in Fig. 12, reveal that there is a large-velocity kink in proximity to the cavity. In Paper I, we showed that such a signature is produced by a stellar mass companion inside the cavity. Deeper and higher spectral resolution observations will help to resolve the nature of these perturbations.

5 SUMMARY

Circumbinary discs generate diverse kinematic and morphological features, some of which are observed in transitional discs that are not yet known to be circumbinary. By using simulations and synthetic observations, we have shown that Doppler-flips, spiral arms, and vortex-like features can appear in the velocity residuals and potentially be misinterpreted as evidence for planet–disc interactions. Two of these features have previously been reported in transition discs. First, vortex-like kinematics were reported by Boehler et al. (2021) spatially colocated with the dust trap in HD 142527. We show in Section 4.1 that the vortex-like kinematics can be reproduced in a circumbinary disc model that does not contain a vortex. The complexity of the kinematics of circumbinary discs means that it will be difficult to be confidently attribute velocity perturbations inside of the dust trap to vortical motion. Second, a Doppler-flip in the disc around HD 100546 was reported by Pérez et al. (2020) and attributed to a multi-Jupiter mass planet. Recently, Casassus et al. (2022) attribute the Doppler-flip to a mass eruption event from a ~ 10 ME planet. In Section 4.2, we show that an eccentric internal companion can reproduce the observed Doppler-flip, as well as other significant velocity perturbations around the central cavity.

Additionally, we analyse the rotation curves of 16 protoplanetary and transitional discs in the literature. We show that two transition discs, AB Aur and HD 100546, have highly perturbed rotation curves inside of their cavities, which may be consistent with our proposition that such perturbations are generated by massive (i.e. above planetary mass) companions. Other transition discs, such as J1604 and LkCa 15 have peculiar kinematic signatures inside of their cavities which appear consistent with companion–disc interactions.

The gas kinematics of transition discs can reveal what physical mechanism is responsible for their origin. A sizeable and high-fidelity sample, such as that soon to be released by the EXOALMA¹ survey, will allow for a more detailed study on the statistical properties of the kinematic perturbations seen inside the cavities of transition discs.

ACKNOWLEDGEMENTS

We thank the anonymous referee for their useful comments which helped improved the clarity of the manuscript. This work is supported by the National Natural Science Foundation of China under grant

no. 12233004 and 12250610189. JeS is supported by the Natural Sciences and Engineering Research Council of Canada (NSERC). DJP and CP are grateful for Australian Research Council funding via DP180104235, DP220103767, and DP240103290. JoS has received funding from the European Research Council (ERC) under the European Union’s Horizon 2020 research and innovation programme (PROTOPLANETS, grant agreement no. 101002188). This paper makes use of ALMA data with project IDs listed in Table 2. ALMA is a partnership of ESO (representing its member states), NSF (USA), and NINS (Japan), together with NRC (Canada), MOST, and ASIAA (Taiwan), and KASI (Republic of Korea), in cooperation with the Republic of Chile. The Joint ALMA Observatory is operated by ESO, AUI/NRAO and NAOJ.

DATA AVAILABILITY STATEMENT

The simulation dump files and selected radiative transfer models will be made available at [10.5281/zenodo.10706132](https://zenodo.org/record/10706132). Observational data from MAPS can be obtained from <https://alma-maps.info/data.html>. Additional observational data can be found in the citations in the caption of Table 2, or by contacting the authors. PHANTOM is publicly available at <https://github.com/danieljprice/phantom>, while MCFOST is available at <https://github.com/cpinte/mcfost>.

REFERENCES

- Allard F., Hauschildt P. H., Alexander D. R., Tamanai A., Schweitzer A., 2001, *ApJ*, 556, 357
- Ataiee S., Pinilla P., Zsom A., Dullemond C. P., Dominik C., Ghanbari J., 2013, *A&A*, 553, L3
- Avenhaus H., Quanz S. P., Schmid H. M., Meyer M. R., Garufi A., Wolf S., Dominik C., 2014, *ApJ*, 781, 87
- Avenhaus H. et al., 2017, *AJ*, 154, 33
- Bae J., Isella A., Zhu Z., Martin R., Okuzumi S., Suriano S., 2023, in Inutsuka S., Aikawa Y., Muto T., Tomida K., Tamura M., eds, ASP Conf. Ser. Vol. 534, Protostars and Planets VII. Astron. Soc. Pac., San Francisco, p. 423
- Bate M. R., Bonnell I. A., Price N. M., 1995, *MNRAS*, 277, 362
- Biddle L. I., Bowler B. P., Zhou Y., Franson K., Zhang Z., 2024, *ApJ*, 167, 10
- Biller B. et al., 2012, *ApJ*, 753, L38
- Boehler Y. et al., 2021, *A&A*, 650, A59
- Bollati F., Lodato G., Price D. J., Pinte C., 2021, *MNRAS*, 504, 5444
- Booth A. S., Walsh C., Kama M., Loomis R. A., Maud L. T., Juhász A., 2018, *A&A*, 611, A16
- Booth A. S., Ilee J. D., Walsh C., Kama M., Keyte L., van Dishoeck E. F., Nomura H., 2023, *A&A*, 669, A53
- Brittain S. D., Carr J. S., Najita J. R., Quanz S. P., Meyer M. R., 2014, *ApJ*, 791, 136
- Brittain S. D., Najita J. R., Carr J. S., 2019, *ApJ*, 883, 37
- Calcino J., Price D. J., Pinte C., van der Marel N., Ragusa E., Dipierro G., Cuello N., Christiaens V., 2019, *MNRAS*, 490, 2579
- Calcino J., Hilder T., Price D. J., Pinte C., Bollati F., Lodato G., Norfolk B. J., 2022, *ApJ*, 929, L25
- Calcino J., Price D. J., Pinte C., Garg H., Norfolk B. J., Christiaens V., Li H., Teague R., 2023, *MNRAS*, 523, 5763
- Casassus S., Pérez S., 2019, *ApJ*, 883, L41
- Casassus S. et al., 2013, *Nature*, 493, 191
- Casassus S. et al., 2015, *ApJ*, 812, 126
- Casassus S., Cárcamo M., Hales A., Weber P., Dent B., 2022, *ApJ*, 933, L4
- Christiaens V., Casassus S., Pérez S., van der Plas G., Ménard F., 2014, *ApJ*, 785, L12
- Christiaens V. et al., 2018, *A&A*, 617, A37
- Close L. M. et al., 2014, *ApJ*, 781, L30
- Cornwell T. J., 2008, *IEEE J. Sel. Top. Signal Process.*, 2, 793
- Currie T., 2024, *Res. Notes Am. Astron. Soc.*, 8, 146

¹<https://www.exoalma.com/>

- Currie T., Cloutier R., Brittain S., Grady C., Burrows A., Muto T., Kenyon S. J., Kuchner M. J., 2015, *ApJ*, 814, L27
- Currie T. et al., 2022, *Nat. Astron.*, 6, 751
- Dipierro G., Price D., Laibe G., Hirsh K., Cerioli A., Lodato G., 2015, *MNRAS*, 453, L73
- Disk Dynamics Collaboration, 2020, preprint (arXiv:2009.04345)
- Dong R. et al., 2018a, *ApJ*, 860, L24
- Dong R., Najita J. R., Brittain S., 2018b, *ApJ*, 862, 103
- Facchini S. et al., 2020, *A&A*, 639, A121
- Fedele D., Toci C., Maud L., Lodato G., 2021, *A&A*, 651, A90
- Francis L., van der Marel N., 2020, *ApJ*, 892, 111
- Fukagawa M., Tamura M., Itoh Y., Kudo T., Imaeda Y., Oasa Y., Hayashi S. S., Hayashi M., 2006, *ApJ*, 636, L153
- Garg H. et al., 2021, *MNRAS*, 504, 782
- Garg H. et al., 2022, *MNRAS*, 517, 5942
- Guenther E. W., Esposito M., Mundt R., Covino E., Alcalá J. M., Cusano F., Stecklum B., 2007, *A&A*, 467, 1147
- Hall C. et al., 2020, *ApJ*, 904, 8
- Hirsh K., Price D. J., Gonzalez J.-F., Ubeira-Gabellini M. G., Ragusa E., 2020, *MNRAS*, 498, 2936
- Huang P., Isella A., Li H., Li S., Ji J., 2018, *ApJ*, 867, 3
- Huang J. et al., 2021, *ApJS*, 257, 19
- Izquierdo A. F., Testi L., Facchini S., Rosotti G. P., van Dishoeck E. F., 2021, *A&A*, 650, A179
- Izquierdo A. F., Testi L., Facchini S., Rosotti G. P., van Dishoeck E. F., Wölfer L., Paneque-Carreño T., 2023, *A&A*, 674, A113
- Jorsater S., van Moorsel G. A., 1995, *AJ*, 110, 2037
- Kennedy G. M. et al., 2019, *Nat. Astron.*, 3, 230
- Kuo I. H. G., Yen H.-W., Gu P.-G., Chang T.-E., 2022, *ApJ*, 938, 50
- Kurtovic N. T. et al., 2022, *A&A*, 664, A151
- Kutra T., Wu Y., Lithwick Y., 2023, *ApJ*, 964, 14
- Lacour S. et al., 2016, *A&A*, 590, A90
- Law C. J. et al., 2021, *ApJS*, 257, 4
- Law C. J. et al., 2022, *ApJ*, 932, 24
- Leinert C., Zinnecker H., Weitzel N., Christou J., Ridgway S. T., Jameson R., Haas M., Lenzen R., 1993, *A&A*, 278, 129
- Lodato G., Price D. J., 2010, *MNRAS*, 405, 1212
- Lodato G. et al., 2023, *MNRAS*, 518, 4481
- Longarini C., Lodato G., Toci C., Veronesi B., Hall C., Dong R., Patrick Terry J., 2021, *ApJ*, 920, L41
- Melon Fuksman J. D., Klahr H., 2022, *ApJ*, 936, 16
- Mendigutía I., Fairlamb J., Montesinos B., Oudmaijer R. D., Najita J. R., Brittain S. D., van den Ancker M. E., 2014, *ApJ*, 790, 21
- Monaghan J. J., 1992, *ARA&A*, 30, 543
- Nguyen D. C., Brandeker A., van Kerkwijk M. H., Jayawardhana R., 2012, *ApJ*, 745, 119
- Norfolk B. J. et al., 2021, *MNRAS*, 502, 5779
- Norfolk B. J. et al., 2022, *ApJ*, 936, L4
- Nowak M., Rowther S., Lacour S., Meru F., Nealon R., Price D. J., 2024, *A&A*, 683, 11
- Öberg K. I. et al., 2021, *ApJS*, 257, 1
- Ohashi N., 2008, *Ap&SS*, 313, 101
- Paneque-Carreño T. et al., 2021, *ApJ*, 914, 88
- Pavlyuchenkov Y. N., Maksimova L. A., Akimkin V. V., 2022, *Astron. Rep.*, 66, 800
- Perez S. et al., 2015a, *ApJ*, 798, 85
- Perez S., Dunhill A., Casassus S., Roman P., Szulágyi J., Flores C., Marino S., Montesinos M., 2015b, *ApJ*, 811, L5
- Pérez S., Casassus S., Benítez-Llambay P., 2018, *MNRAS*, 480, L12
- Pérez S. et al., 2020, *ApJ*, 889, L24
- Phuong N. T. et al., 2020, *A&A*, 635, L9
- Pineda J. E. et al., 2019, *ApJ*, 871, 48
- Pinte C., Ménard F., Duchêne G., Bastien P., 2006, *A&A*, 459, 797
- Pinte C., Harries T. J., Min M., Watson A. M., Dullemond C. P., Woitke P., Ménard F., Durán-Rojas M. C., 2009, *A&A*, 498, 967
- Pinte C. et al., 2018, *ApJ*, 860, L13
- Pinte C. et al., 2019, *Nat. Astron.*, 3, 1109
- Pinte C. et al., 2020, *ApJ*, 890, L9
- Pinte C. et al., 2023a, *MNRAS*, 526, L41
- Pinte C., Teague R., Flaherty K., Hall C., Facchini S., Casassus S., 2023b, in Inutsuka S., Aikawa Y., Muto T., Tomida K., Tamura M., eds, *ASP Conf. Ser. Vol. 534, Protostars and Planets VII*. Astron. Soc. Pac., San Francisco, p. 645
- Poblete P. P., Cuello N., Cuadra J., 2019, *MNRAS*, 489, 2204
- Price D. J. et al., 2018a, *PASA*, 35, e031
- Price D. J. et al., 2018b, *MNRAS*, 477, 1270
- Quanz S. P., Avenhaus H., Buenzli E., Garufi A., Schmid H. M., Wolf S., 2013, *ApJ*, 766, L2
- Rabago I., Zhu Z., Martin R. G., Lubow S. H., 2023, *MNRAS*, 520, 2138
- Rafikov R. R., 2002, *ApJ*, 569, 997
- Ragusa E., Dipierro G., Lodato G., Laibe G., Price D. J., 2017, *MNRAS*, 464, 1449
- Ragusa E., Alexander R., Calcino J., Hirsh K., Price D. J., 2020, *MNRAS*, 499, 3362
- Ragusa E., Lynch E., Laibe G., Longarini C., Ceppi S., 2024, *A&A*, 686, A264
- Rivière-Marichalar P., Fuente A., Baruteau C., Neri R., Treviño-Morales S. P., Carmona A., Agúndez M., Bachiller R., 2019, *ApJ*, 879, L14
- Rivière-Marichalar P. et al., 2020, *A&A*, 642, A32
- Robert C. M. T., Méheut H., Ménard F., 2020, *A&A*, 641, A128
- Shakura N. I., Sunyaev R. A., 1973, *A&A*, 24, 337
- Siess L., Dufour E., Forestini M., 2000, *A&A*, 358, 593
- Sissa E. et al., 2018, *A&A*, 619, A160
- Speedie J., Booth R. A., Dong R., 2022, *ApJ*, 930, 40
- Stadler J. et al., 2023, *A&A*, 670, L1
- Stolker T. et al., 2023, *A&A*, 682, 20
- Suriano S. S., Li Z.-Y., Krasnopolsky R., Shang H., 2018, *MNRAS*, 477, 1239
- Teague R., 2019, *J. Open Source Softw.*, 4, 1220
- Teague R., Foreman-Mackey D., 2018, bettermoments: A robust method to measure line centroids. Zenodo, <https://doi.org/10.5281/zenodo.1419754>
- Teague R., Bae J., Bergin E. A., Birnstiel T., Foreman-Mackey D., 2018, *ApJ*, 860, L12
- Teague R., Bae J., Bergin E. A., 2019, *Nature*, 574, 378
- Teague R. et al., 2021, *ApJS*, 257, 18
- Teague R. et al., 2022, *ApJ*, 936, 163
- Terry J. P., Hall C., Longarini C., Lodato G., Toci C., Veronesi B., Paneque-Carreño T., Pinte C., 2021, *MNRAS*, 510, 1671
- Veronesi B., Paneque-Carreño T., Lodato G., Testi L., Pérez L. M., Bertin G., Hall C., 2021, *ApJ*, 914, L27
- Verrios H. J., Price D. J., Pinte C., Hilder T., Calcino J., 2022, *ApJ*, 934, L11
- Vioque M., Oudmaijer R. D., Baines D., Mendigutía I., Pérez-Martínez R., 2018, *A&A*, 620, A128
- Walsh C. et al., 2014, *ApJ*, 791, L6
- Wölfer L. et al., 2021, *A&A*, 648, A19
- Wölfer L. et al., 2023, *A&A*, 670, A154
- Wright C. M. et al., 2015, *MNRAS*, 453, 414
- Wu Y., Lithwick Y., 2021, *ApJ*, 923, 123
- Yang H., Fernandez-Lopez M., Li Z.-Y., Stephens I. W., Looney L. W., Lin Z.-Y. D., Harrison R., 2023, *ApJ*, 948, L2
- Zhang K., Blake G. A., Bergin E. A., 2015, *ApJ*, 806, L7
- Zhou Y. et al., 2023, *AJ*, 166, 220
- Zhu Z., Baruteau C., 2016, *MNRAS*, 458, 3918
- Zhu Z., Dong R., Stone J. M., Rafikov R. R., 2015, *ApJ*, 813, 88

This paper has been typeset from a $\text{\TeX}/\text{\LaTeX}$ file prepared by the author.